Nanoscale

PAPER

Published on 17 December 2024
Licence and permissions

Check for updates

Cite this: *Nanoscale*, 2025, **17**, 7253

Exploring the electronic and mechanical properties of the recently synthesized nitrogen-doped amorphous monolayer carbon

Emanuel J. A. dos Santos,[a,b] Marcelo L. Pereira, Junior, *[c] Raphael M. Tromer,[d] Douglas S. Galvão[e] and Luiz A. Ribeiro, Junior [a,b]

Received 17th October 2024,
Accepted 6th December 2024

DOI: 10.1039/d4nr04305g

rsc.li/nanoscale

The recent synthesis of nitrogen-doped amorphous monolayer carbon (NAMC) opens new possibilities for multifunctional materials. In this study, we have investigated the nitrogen doping limits and their effects on NAMC's structural and electronic properties using density functional-based tight-binding simulations. Our results show that NAMC remains stable up to 35% nitrogen doping, beyond which the lattice becomes unstable. The formation energies of NAMC are higher than those of nitrogen-doped graphene for all the cases we have investigated. Both undoped MAC and NAMC exhibit metallic behavior, although only MAC features a Dirac-like cone. MAC has an estimated Young's modulus value of about 410 GPa, while NAMC's modulus can vary around 416 GPa depending on nitrogen content. MAC displays optical activity in the ultraviolet range, whereas NAMC features light absorption within the infrared and visible ranges, suggesting potential for distinct optoelectronic applications. Their structural thermal stabilities were addressed through molecular dynamics simulations. MAC melts at approximately 4900 K, while NAMC loses its structural integrity for temperatures ranging from 300 K to 3300 K, lower than graphene. These results point to potential NAMC applications in flexible electronics and optoelectronics.

1 Introduction

Two-dimensional (2D) carbon-based materials,[1] particularly graphene,[2] have received significant attention over the past decades due to their exceptional mechanical, electronic, and optical properties.[3] Graphene, a monolayer of sp^2-hybridized carbon atoms arranged in a honeycomb lattice, has become a cornerstone for developing flexible electronics, energy storage devices, and other applications.[4] The discovery of graphene has renewed the search for other 2D carbon allotropes, aiming to explore new physical properties and functionalities by modifying the carbon lattice.[5–8] Among these new materials, pure[9,10] and doped[11,12] amorphous 2D carbon lattices have emerged as promising candidates due to their inherent structural flexibility and tunable electronic characteristics. Ref. 12 discusses the effects of different dopants on similar amorphous carbon-based systems, highlighting their unique contributions to material properties. It was shown that boron doping in amorphous carbon tends to reduce the bandgap and improve p-type conductivity due to boron's ability to create acceptor levels near the valence band edge. Similarly, nitrogen doping introduces localized electronic states and enhances light absorption in specific wavelength ranges, which could benefit optoelectronic applications.

The recent synthesis of the first freestanding monolayer of amorphous carbon (MAC) using laser-assisted chemical vapor deposition represents a significant advancement in the field of 2D materials.[9] MAC consists of a random arrangement of sp^2 and sp^3-like hybridized carbon atoms, forming a network of five- to eight-member rings. Unlike graphene's crystalline structure, MAC exhibits short-range order with a wide variation in bond lengths and angles, profoundly influencing its mechanical and electronic properties. A key aspect of this synthesis method is its self-limiting nature, which enabled the rapid formation of a uniform monolayer within minutes, covering several square centimeters, at relatively low substrate temperatures of around 200 °C. This starkly contrasts other techniques that require temperatures as high as 900 °C for amorphous carbon monolayer formation.[13]

MAC's unique ring distribution deviates from conventional Zachariasen random networks,[13] endowing it with exceptional thermal stability and mechanical strength.[14,15] This structural

[a]*University of Brasília, Institute of Physics, Brasília, Federal District, Brazil*
[b]*Computational Materials Laboratory, LCCMat, Institute of Physics, University of Brasília, Brasília, Brazil*
[c]*University of Brasília, College of Technology, Department of Electrical Engineering, Brasília, Federal District, Brazil. E-mail: marcelo.lopes@unb.br*
[d]*School of Engineering, MackGraphe, Mackenzie Presbyterian University, São Paulo, Brazil*
[e]*Department of Applied Physics and Center for Computational Engineering and Sciences, State University of Campinas, Campinas, São Paulo, Brazil*

disorder, while different from graphene, offers distinct advantages. As a result, MAC holds great promise for a range of applications, including flexible electronics,[16] energy storage,[17] and optoelectronics.[18] While it shares some of the beneficial properties of graphene,[19] MAC's structural disorder introduces additional functionalities that make it an attractive candidate for future technologies.

The recent synthesis of nitrogen-doped amorphous monolayer carbon (NAMC) introduces another exciting development in two-dimensional materials.[11] NAMC was synthesized through a space-confined solution-phase process using a layered double hydroxide (LDH) template, facilitating precise control over nitrogen incorporation into the amorphous carbon lattice. This novel approach yields a freestanding monolayer consisting of a random arrangement of five-, six-, and seven-membered carbon rings, where nitrogen atoms replace some of the carbon atoms within the network. The polymerization of pyrrole within the confined interlayer of the LDH template is critical to forming the nitrogen-doped structure, preventing excessive bond rearrangements that could lead to instability during synthesis. As a result, NAMC exhibits a unique in-plane π-like-conjugation electronic structure, setting it apart from other carbon-based 2D materials. Nitrogen atoms further impact the material's electronic and mechanical properties by introducing localized electronic states distinct from those observed in pure amorphous carbon or crystalline graphene.[11] Additionally, the nitrogen-doped structure maintains the flexibility and structural disorder characteristic of amorphous carbon while offering enhanced tunability of its electronic and optical properties through controlling nitrogen content.[11] These features make NAMC a promising candidate for applications in flexible electronics, optoelectronics, and other multifunctional devices, where structural flexibility and controlled electronic behavior are critical.

Nitrogen doping is a well-known strategy for tuning the properties of carbon-based materials,[20–23] providing enhanced control over electronic behavior,[24] mechanical strength,[25,26] and chemical reactivity.[27,28] However, the critical issue of the nitrogen saturation limit that can be incorporated into the amorphous carbon lattice while maintaining its structural integrity remains to be determined. Understanding this doping limit is crucial for optimizing NAMC sheets for various applications, particularly in flexible electronics and optoelectronics, where precise control over material properties is essential.

In this study, we have addressed this fundamental question through density functional-based tight-binding (DFTB+) simulations. Molecular dynamics (MD) simulations were also carried out to investigate the nitrogen doping limits in NAMC and their effects on the material's structural, optical, mechanical, and electronic properties. Our findings revealed that NAMC remains structurally stable up to a nitrogen doping concentration of 35%, beyond which the lattice becomes unstable. Furthermore, we have also analyzed these properties for nitrogen-doped graphene (N-Gr) and NAMC to understand how nitrogen incorporation comprehensively alters their behavior.

2 Methodology

In this study, we have used DFTB+ simulations[29,30] to explore the structural, electronic, and mechanical properties of MAC and NAMC with different nitrogen-doping contents. The 3ob set of Slater–Koster parameters,[31,32] and dispersion correction were adopted for the calculations. Importantly, although providing lower precision results than pure DFT methods, DFTB+ can produce good-quality results for treating large-scale systems, which would be cost-prohibitive with pure DFT methods. This is particularly important for modeling the disordered structure of monolayer amorphous carbon, which typically requires large unit cells.

The DFTB+ method relies on pre-calculated integrals and parametrized Hamiltonians derived from DFT calculations for reference systems.[29,33] These parametrizations capture the essential chemical interactions between atoms, allowing DFTB+ to describe bonding, electronic states, and structural properties accurately.[34–36] Additionally, DFTB+ supports efficient geometry optimizations and molecular dynamics simulations, providing insights into equilibrium properties and dynamic behaviors at various temperatures.[37–39]

An essential feature of DFTB+ is its ability to account for self-consistent charge redistribution, which becomes crucial when dealing with heteroatomic systems such as NAMC.[29,30] Nitrogen doping introduces localized electronic states and charge polarization effects within the carbon network, which DFTB+ captures through its self-consistent charge formalism.[40–42] This capability allows us to accurately model the impact of nitrogen on the structural stability, electronic properties, and mechanical behavior of NAMC across different doping concentrations. Thus, DFTB+ strikes an optimal balance between computational efficiency and accuracy, making it a powerful tool for studying complex amorphous carbon-based systems.[43–46]

In our approach, MAC, N-Gr, and NAMC structural models (PM-CS-1 space group) contain 100 total atoms and were created based on the available experimental data[11] (see Fig. 1). The lattice vectors $\vec{a}$ and $\vec{b}$ are 15.00 Å and 20.42 Å, respectively. These models consist of randomly distributed five-, six-, and seven-membered carbon rings and nitrogen-doping sites, forming the MAC and NAMC sheets. The nitrogen doping process was simulated by randomly replacing carbon atoms with nitrogen ones at different concentrations, ranging from 5% up to 40% of the total number of carbon atoms. Fig. 1 illustrates the model lattices studied in this work, *i.e.*, the (a) MAC, (b) NAMC structure doped with 10% nitrogen (N_{10}AMC), and (c) NAMC structure doped with 35% nitrogen (N_{35}AMC).

The geometry optimizations were performed using the DFTB+ package for each nitrogen-doped structure. The convergence criteria for structure optimization and energy calculation were set to energy tolerance of 0.02 kcal mol^{-1}, maximum force tolerance of 0.1 kcal mol^{-1} $Å^{-1}$, and maximum displacement tolerance of 0.001 Å, ensuring that each system was in its lowest energy state. Periodic boundary conditions were applied to mimic the behavior of an infinite

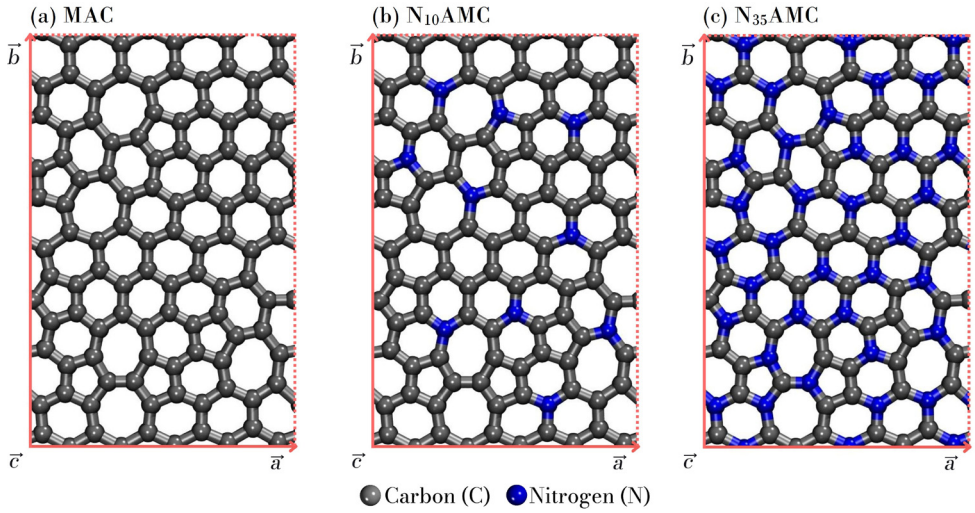

Fig. 1 Schematic representation of some of the proposed structural models with their corresponding lattice vectors. (a) Pure amorphous monolayer carbon (MAC), (b) NAMC structure doped with 10% nitrogen, and (c) NAMC structure doped with 35% nitrogen.

monolayer. The optimized geometries were then used to analyze the electronic and mechanical properties of the MAC and NAMC systems.

The electronic and optical properties were also computed, including the electronic band structure, the projected density of states (DOS), charge distribution, and light absorption coefficient. The Monkhorst–Pack scheme was employed to sample the Brillouin zone with a 15 × 15 × 1 *k*-point grid for accurate results. The mechanical properties of the nitrogen-doped amorphous monolayer carbon were assessed by calculating Young's modulus and Poisson's ratio for each optimized structure. Special attention was dedicated to the effects of nitrogen doping on the electronic characteristics of the NAMC systems, particularly on the bandgap values and the presence or absence of Dirac-like cones.

To further explore the thermal stability of MAC and NAMC layers, we also carried out MD simulations using DFTB+. These simulations were performed under the NVT ensemble using a time step of 1 fs and a Nosé–Hoover thermostat[47] to control the temperature values. The systems were incrementally heated from 10 K to 5000 K to determine their melting points.

DFTB+ provides a reliable and computationally efficient approach for investigating NAMC structural and electronic properties. The accuracy of DFTB+ for systems containing carbon–carbon and carbon–nitrogen bonds has been extensively validated in the literature, demonstrating excellent agreement with DFT calculations.[29,48,49] This agreement is consistent across systems with varying degrees of crystallinity, including amorphous and defective carbon materials.[50,51] Additionally, DFTB+ has proven effective in accurately modeling charge distribution and local bonding environments for nitrogen doping, further supporting its suitability for our study.[51] By enabling simulations of larger systems and longer time scales than those feasible with DFT, DFTB+ ensures the exploration of complex doping scenarios while maintaining computational tractability.[52]

3 Results

We begin the discussions by analyzing the structural results for N-Gr and NAMC. The formation energy, $E_F(n)$, as a function of n doping concentration, is defined by

$$E_F(n) = \frac{E_{N_n AMC} - n \cdot E_N - (100 - n) \cdot E_C}{100}, \quad (1)$$

where $E_{N_n\ AMC}$ is the total energy of the NAMC and E_N and E_C are the nitrogen and carbon atoms isolated-energy, respectively. As shown in Fig. 2, the E_F of NAMC is consistently higher than that of N-Gr for all nitrogen contents investigated here. This difference arises from the intrinsic structural characteristics of the two materials. Graphene possesses a highly ordered hexagonal lattice, allowing for uniform incorporation of nitrogen atoms with minimal structural disruption to the bonding network. In contrast, MAC exhibits a disordered structure composed of a mixture of five-, six-, and seven-membered carbon rings, which leads to variations in bond lengths and angles. When nitrogen atoms are introduced into the disordered MAC lattice, they disrupt the local bonding environment more significantly than in the regular structure of graphene.

Also, nitrogen atoms have different atomic radii and bonding configurations than carbon ones. As the lattice has to accommodate more nitrogen atoms at higher doping concentrations, it results in more pronounced bond distortions and increased residual strain throughout the structure. This additional strain increases the formation energy values as the lattice becomes progressively less stable with increasing nitrogen content.

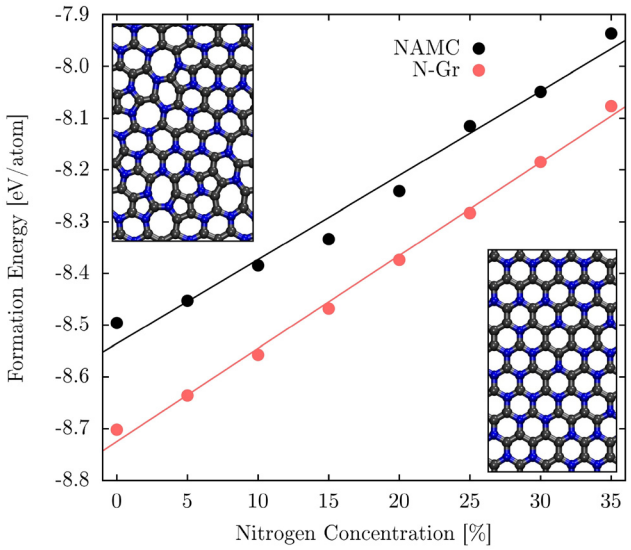

Fig. 2 Formation energy values as a function of nitrogen concentration (N%) for NAMC (black) and N-Gr (red). The insets depict the atomic structures of the NAMC (left) and N-Gr (right) systems, with the nitrogen atoms highlighted in blue.

Although for N-Gr and NAMC, the increase in formation energy values allows a good linear fitting with nitrogen concentration, their behavior is slightly different. For N-Gr, the fitting is almost perfectly linear, with a rate of change of 0.018 eV per atom per unit of nitrogen concentration, with an error of 2.6%, reflecting the uniform nature of its hexagonal carbon lattice. The ordered structure of graphene allows for an easier adjustment to nitrogen incorporation, resulting in a steady increase in formation energy with each incremental increase in doping concentration. In contrast, NAMC shows a slight deviation from ideal linearity, with some dispersion among data points. For NAMC, the increase in energy as a function of doping concentration has a growth rate of 0.016 eV per atom, with a 5.8% error in fitting the data points. This deviation arises from the amorphous nature of the MAC lattice, where variations in local atomic environments lead to uneven strain distributions as nitrogen atoms are incorporated. The intrinsic disorder of MAC introduces variations in how nitrogen atoms interact with the surrounding carbon network, resulting in differences in the energy values required to stabilize the structure at different doping levels. Importantly, we observed that the reported formation energies and structural features align well with values documented in the literature for nitrogen-free amorphous carbon.[12,53,54] This consistency underscores the reliability of DFTB+ for capturing critical properties of NAMC.

The results further reveal that the nitrogen doping limit for maintaining lattice structural stability in NAMC is 35%. Doping levels up to 35% yield negative formation energies, indicating stability, while higher concentrations result in positive formation energies, pointing to instability. In contrast, graphene can accommodate a higher nitrogen concentration before becoming unstable.[55] This difference is primarily attributed to the structural characteristics of MAC, which, unlike graphene, lacks uniformity and long-range order.[9–11] The disordered arrangement of carbon rings in MAC results in a structure that experiences significant structural deformations at elevated doping levels. As discussed above, as more nitrogen atoms are incorporated into the structures, there is an increase in strain, which contributes to significant structural distortions. In contrast, the regular hexagonal lattice of graphene offers a more stable framework for nitrogen incorporation, enabling the material to sustain higher doping levels without compromising its structural integrity.

Based on the formation energy and structural analyses, we selected two relevant nitrogen doping concentrations for a more detailed investigation: 10% and 35%. The 10% doping level was chosen to align with the concentration reported in the experimental synthesis of NAMC.[11] This choice allows for a direct comparison between our theoretical predictions and experimental observations, providing a deeper understanding of NAMC's properties at a moderate doping concentration. In contrast, the 35% doping level was selected because it represents the upper limit of nitrogen concentration at which the NAMC lattice remains stable, offering insights into the structural and electronic behavior of the material at the highest achievable doping level without compromising lattice structural stability.

Similar behavior has been reported in other studies of nitrogen-doped carbon materials.[56–60] For instance, studies on nitrogen-doped tetrahedral amorphous carbon (ta-C) have demonstrated that while low levels of nitrogen incorporation can be accommodated, higher concentrations lead to significant changes in bonding configurations and increased defect densities, resulting in structural instability.[60] These findings suggest that the introduction of nitrogen into amorphous carbon structures is limited by the material's ability to accommodate the resulting strain and disorder. Beyond a specific doping concentration, the accumulation of defects and the disruption of the carbon network's integrity lead to instability. Therefore, our study's 35% nitrogen doping threshold aligns with these observations, indicating a critical limit for maintaining structural stability in nitrogen-doped amorphous carbon materials.

The electronic band structure features change as nitrogen atoms are incorporated into the MAC lattice. For the N_{10}AMC case (Fig. 3(b)), the Dirac-like cone observed in undoped MAC disappears. This change can be attributed to the delocalized π-electron network disruption caused by nitrogen substitution. Due to their distinct number of electrons and bond nature compared to carbon, nitrogen atoms introduce localized electronic states into the band structure. These localized states disrupt the symmetry that initially enabled the appearance of the Dirac-like cone in the undoped MAC. The PDOS for NAMC with 10% nitrogen shows that carbon p-orbitals dominate the contributions to electronic states near the Fermi level. In contrast, the nitrogen p-orbitals contribute only marginally. This trend indicates that, at this doping level, nitrogen primarily acts as a perturbative element in the electronic structure rather

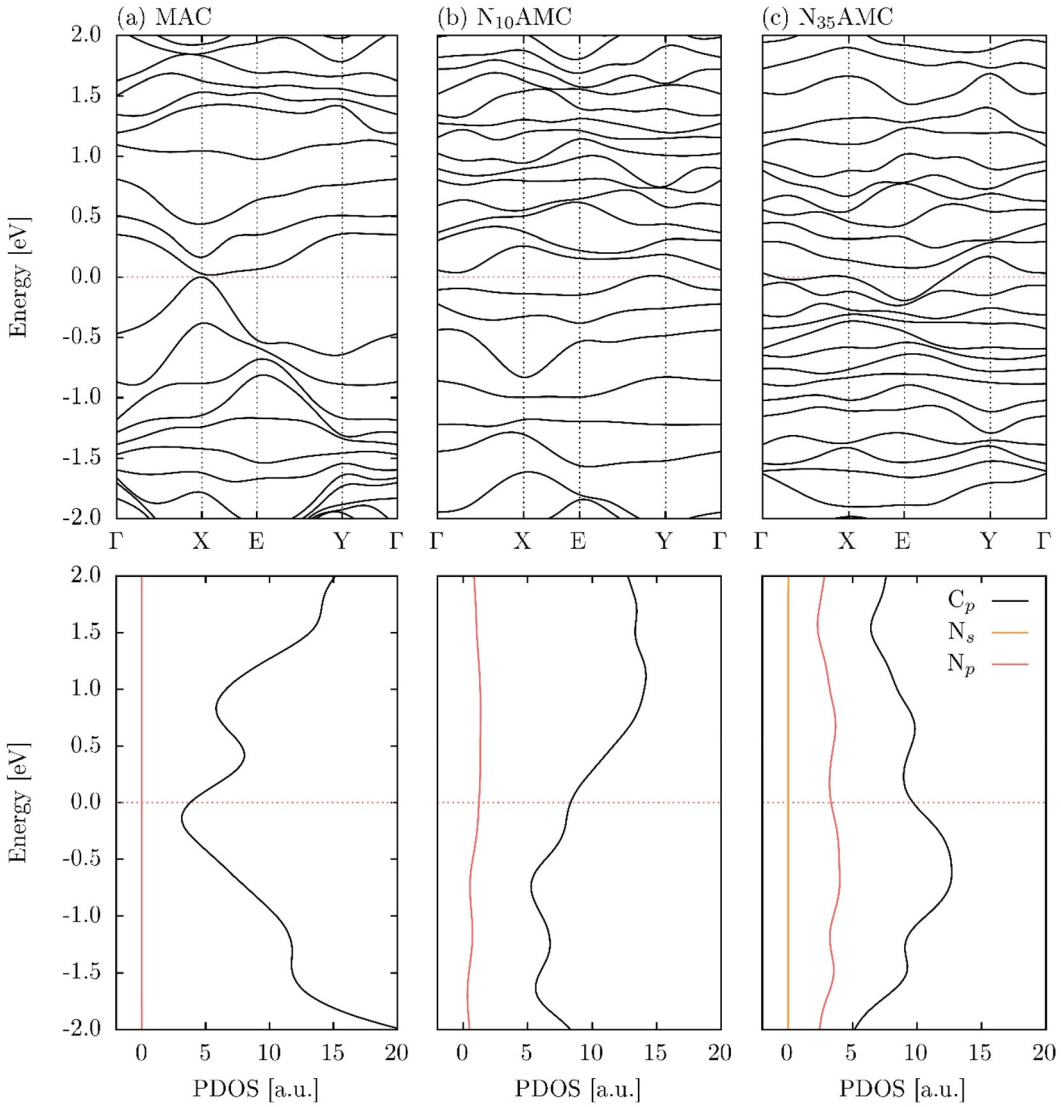

Fig. 3 Electronic band structure and projected density of states (PDOS) for (a) MAC, (b) N_{10}AMC, and (c) N_{35}AMC. The red dashed line indicates the Fermi level.

than playing a significant role in the material's conduction mechanism.

In contrast, the electronic band structure of the NAMC system with 35% nitrogen doping (Fig. 3(c)) exhibits more pronounced changes. The PDOS for this system reveals relevant contributions from nitrogen's s- and p-orbitals to the electronic states near the Fermi level. This behavior differs from the 10% nitrogen-doped system, where the nitrogen p-orbitals played a more limited role. The increased nitrogen content at 35% leads to a more significant localization of electronic states, particularly those arising from nitrogen's s-orbitals, which hybridize with the carbon p-orbitals to form the bands near the Fermi level. This enhanced hybridization alters the electronic structure, resulting in a distinct band profile compared to the undoped MAC and N_{10}AMC systems.

Fig. 4 illustrates the spatial distribution of the highest occupied crystalline orbital (HOCO, in red) and lowest unoccupied crystalline orbital (LUCO, in green) for the three systems: undoped MAC (Fig. 4(a)), N_{10}AMC (Fig. 4(b)), and N_{35}AMC (Fig. 4(c)). Due to the amorphous nature of these materials, the overall spatial distribution of the HOCO and LUCO lacks a clear or ordered pattern, with distinct contributions from atoms at different parts of the structure. This is characteristic of amorphous materials, where the lack of long-range atomic order leads to localized electronic states.[11] The observed orbital delocalization in undoped MAC aligns closely with findings from previous studies.[12,54,61]

Introducing nitrogen into the MAC structure does not fundamentally alter the spatial distribution of frontier electronic orbitals. However, as shown in Fig. 4(b), regions with more nitrogen atoms tend to exhibit more localized orbitals. This behavior can be attributed to the electronic nature of nitrogen, which is more electronegative than carbon. In areas where nitrogen atoms cluster or are more concentrated, they create

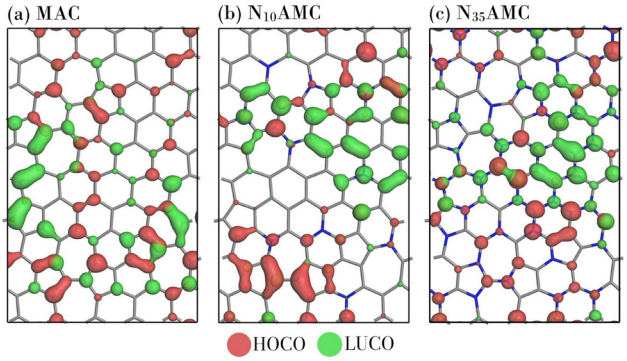

Fig. 4 Spatial distribution of the highest occupied crystalline orbital (HOCO, in red) and lowest unoccupied crystalline orbital (LUCO, in green) for (a) MAC, (b) N_{10}AMC, and (c) N_{35}AMC.

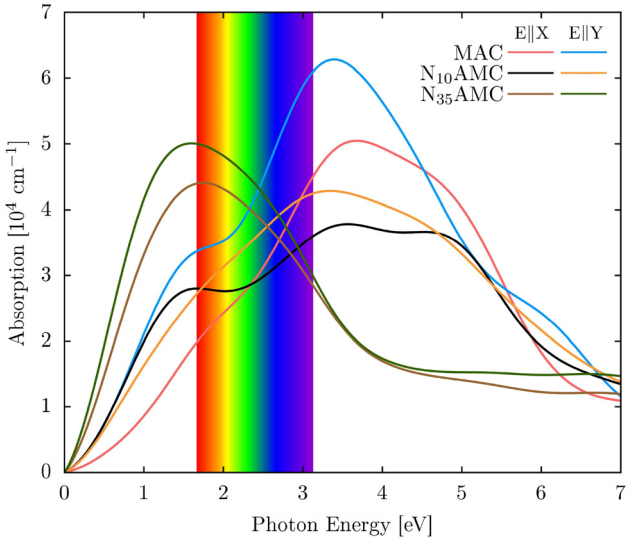

Fig. 5 Optical absorption spectra of (red and blue) MAC, (black and yellow) N_{10}AMC, and (brown and green) N_{35}AMC. The light absorption coefficient is shown as a function of photon energy value, highlighting the influence of nitrogen doping on the optical properties.

localized perturbations in the electronic structure, leading to the confinement of the HOCO and LUCO in those regions. Consequently, these orbitals become more localized around nitrogen-rich areas. Nonetheless, the overall spatial distribution of the orbitals persists due to the amorphous nature of the MAC structure.

At higher nitrogen concentrations, as observed in the NAMC system with 35% doping (Fig. 4(c)), there is an apparent increase in the degree of orbital delocalization. This trend can be explained by the more significant number of nitrogen-induced electronic states interacting with the carbon network. As more nitrogen atoms are incorporated, they create more hybridized states with carbon p-orbitals, resulting in a broader overlap of electronic states. This enhanced hybridization between nitrogen and carbon atomic orbitals increases the coupling of the electronic orbitals throughout the structure, leading to greater delocalization of both the HOCO and LUCO. The more extensive overlap between nitrogen and carbon orbitals allows the electronic states to spread further across the structure, reducing the tendency for orbitals to remain confined to localized regions.

Now, we discuss the optical absorption of the MAC and NAMC systems. In Fig. 5, we present the optical absorption spectra of the undoped MAC (red and blue), N_{10}AMC (black and yellow), and N_{35}AMC (brown and green) for light polarization along the plane (x,y)-directions. The undoped MAC exhibits a strong optical absorption, primarily in the ultraviolet (UV) region. This behavior can be attributed to the nature of the electronic transitions in the all-carbon amorphous network. The delocalized π-electrons in the sp^2 regions of MAC contribute to transitions requiring higher photon energies, which correspond to UV light.

As observed for the NAMC systems, introducing nitrogen into the MAC structure results in a redshift in the absorption spectra. This shift can be attributed to new localized states within the electronic band structure caused by nitrogen incorporation. Due to its higher electronegativity than carbon, nitrogen introduces electronic states closer to the Fermi level, lowering the energy required for electronic transitions. Consequently, lower-energy photons, corresponding to the visible or even infrared regions, become sufficient to induce these transitions, shifting the absorption peak toward longer wavelengths (lower energies). Moreover, nitrogen doping disrupts the sp^2 bonding network of the carbon atoms, increasing light scattering and reducing the intensity of the absorption peaks.

The N_{10}AMC system exhibits an increase/decrease in optical activity in the visible/UV region (black and yellow curves), as shown in Fig. 5. This moderate optical activity arises from a balance between retaining sufficient carbon–carbon π-bonding regions, which continue contributing to UV absorption, and introducing nitrogen states that induce lower-energy transitions. The 10% nitrogen concentration is low enough to preserve some of the intrinsic electronic transitions of undoped MAC while providing enough localized states to extend the absorption into the visible spectrum.

In contrast, the N_{35}AMC system exhibits an absorption spectrum that extends further into the infrared and visible regions (brown and green curves in Fig. 5). At this higher nitrogen concentration, the additional localized states introduced by nitrogen atoms significantly reshape the material's electronic structure. The increased nitrogen content results in a higher density of states near the Fermi level, making low-energy electronic transitions more likely. As a result, the absorption spectrum is dominated by transitions involving these states, leading to optical activity that spans into the infrared and visible regions. This characteristic makes the NAMC system with 35% doping particularly promising for applications that require an optical response in the lower-energy range of the spectrum, such as infrared detectors and specialized optoelectronic devices.

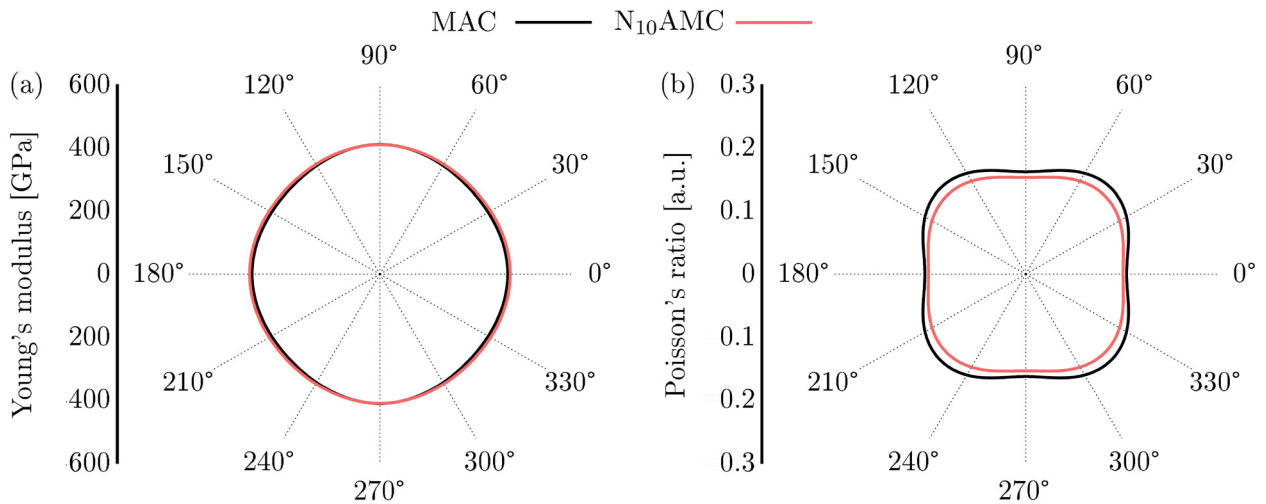

Fig. 6 (a) Estimated Young's modulus and (b) Poisson's ratio values about the basal plane for MAC and N_{10}AMC.

Some of the mechanical properties of the MAC and N_{10}AMC systems are illustrated in Fig. 6. We have estimated Young's modulus ($Y(\theta)$) and Poisson's ratio ($\nu(\theta)$) values under pressure along the xy plane, as given by the following equations:[62,63]

$$Y(\theta) = \frac{C_{11}C_{22} - {C_{12}}^2}{C_{11}\alpha^4 + C_{22}\beta^4 + \left(\frac{C_{11}C_{22} - {C_{12}}^2}{C_{44}} - 2C_{12}\right)\alpha^2\beta^2} \quad (2)$$

and

$$\nu(\theta) = \frac{\left(C_{11} + C_{22} - \frac{C_{11}C_{22} - {C_{12}}^2}{C_{44}}\right)\alpha^2\beta^2 - C_{12}(\alpha^4 + \beta^4)}{C_{11}\alpha^4 + C_{22}\beta^4 + \left(\frac{C_{11}C_{22} - {C_{12}}^2}{C_{44}} - 2C_{12}\right)\alpha^2\beta^2}. \quad (3)$$

Here, $\alpha = \sin(\theta)$, $\beta = \cos(\theta)$, and C_{11}, C_{22}, C_{12}, and C_{44} represent the 2D linear elastic constants. The specific values used to compute these mechanical properties are shown in Table 1, providing key insights into the material's behavior under various types of deformation. Specifically, C_{11} and C_{22} describe the stiffness along different in-plane directions, C_{12} captures the coupling between these directions, and C_{44} characterizes the material's resistance to shear deformation. These constants satisfy the Born–Huang stability criteria – namely, ${C_{11}C_{22} - C_{12}}^2 > 0$ and $C_{44} > 0$ [64,65] – ensuring that both the undoped MAC and N_{10}AMC structures retain their structural stability under strain.

Table 1 Elastic constants C_{ij} (GPa) and maximum values for Young's modulus (GPa) (Y_{max}) and maximum (ν_{max}) and (ν_{min}) Poisson's ratios

Structure	C_{11}	C_{12}	C_{22}	C_{44}	Y_{max}	ν_{max}	ν_{min}
MAC	409.40	66.11	419.95	163.56	405	0.18	0.15
N_{10}AMC	416.43	63.54	418.36	168.94	410	0.17	0.15

It is important to remark that the mechanical properties of the NAMC system with 35% nitrogen doping were not calculated, as this structure is only metastable at 300 K, as discussed below. Due to its instability at room temperature, any mechanical property analysis would not accurately reflect the behavior of a stable lattice. Consequently, we focused our calculations on the undoped MAC and the NAMC system with 10% nitrogen doping, which maintains structural stability under the considered conditions.

In Fig. 6(a), we present the results for Young's modulus for undoped MAC (black) and N_{10}AMC (red). The estimated values are 409.40 GPa and 416.43 GPa, respectively. The volume of the system, required for the calculation of Young's modulus, was considered as $V = l_x \cdot l_y \cdot h_z$, where l_x and l_y represent the in-plane dimensions of the system. At the same time, h_z is the system's thickness, taken here as 3.35 Å, a reference value for graphene.[66] The variation in these values can be attributed to the impact of nitrogen atoms on the structural rigidity of the amorphous carbon network. The well-distributed sp^2 and sp^3-like hybridized carbon atoms in the undoped MAC contribute to a relatively small Young's modulus value. Introducing 10% nitrogen slightly increases this value due to the localized disruptions caused by nitrogen atoms within the carbon lattice and nitrogen–carbon bonds. Nitrogen atoms also introduce distortions and break the uniformity of the carbon–carbon bonding network, increasing the overall stiffness of the structure. These findings agree with an MD study on undoped and nitrogen-doped graphene, in which the latter presenters a slightly higher Young's modulus than the former.[67] This study has also revealed that at some doping levels, up to 6%, Young's modulus of graphene was not changed.[67]

Fig. 6(b) illustrates the Poisson's ratio values for the same set of structures. The all-carbon MAC exhibits a slightly higher Poisson's ratio than its nitrogen-doped counterpart, and a general trend can be inferred where the Poisson's ratio decreases as the nitrogen doping concentration increases. The

Poisson's ratio measures the material's tendency to expand/compress laterally when compressed/stretched longitudinally. The presence of nitrogen atoms alters the local bonding environment and introduces localized regions of stiffness, as mentioned above. This localized stiffness reduces the material's ability to deform laterally under strain, resulting in a lower Poisson's ratio. In both cases, MAC and N_{10}AMC exhibit brittle behavior, regardless of the strain direction, similar to graphene, as $\nu < 0.25$ (ductility criterion).[68] Thus, the increase in the number of rings in the amorphous case and nitrogen doping up to 10% does not alter the fracture pattern observed in the crystalline honeycomb lattice.

The variations in Young's modulus and Poisson's ratio with nitrogen concentration highlight the tunable nature of the mechanical properties in NAMC systems, making them promising candidates for applications where specific mechanical characteristics are required.

Finally, in Fig. 7, we present the results from the MD simulations, showcasing the thermal stability of the MAC and NAMC systems, with representative snapshots taken at different temperatures. The top, middle, and bottom rows correspond to the undoped MAC, N_{10}AMC, and N_{35}AMC cases. These simulations provide valuable insights into these materials' structural integrity under increasing temperatures.

The undoped MAC (top row) and N_{10}AMC (middle row) demonstrate thermal stability at room temperature, maintaining their structural integrity. The undoped MAC and N_{10}AMC become thermally unstable at 3800 K and 3300 K, respectively. This difference can be attributed to nitrogen atoms in the

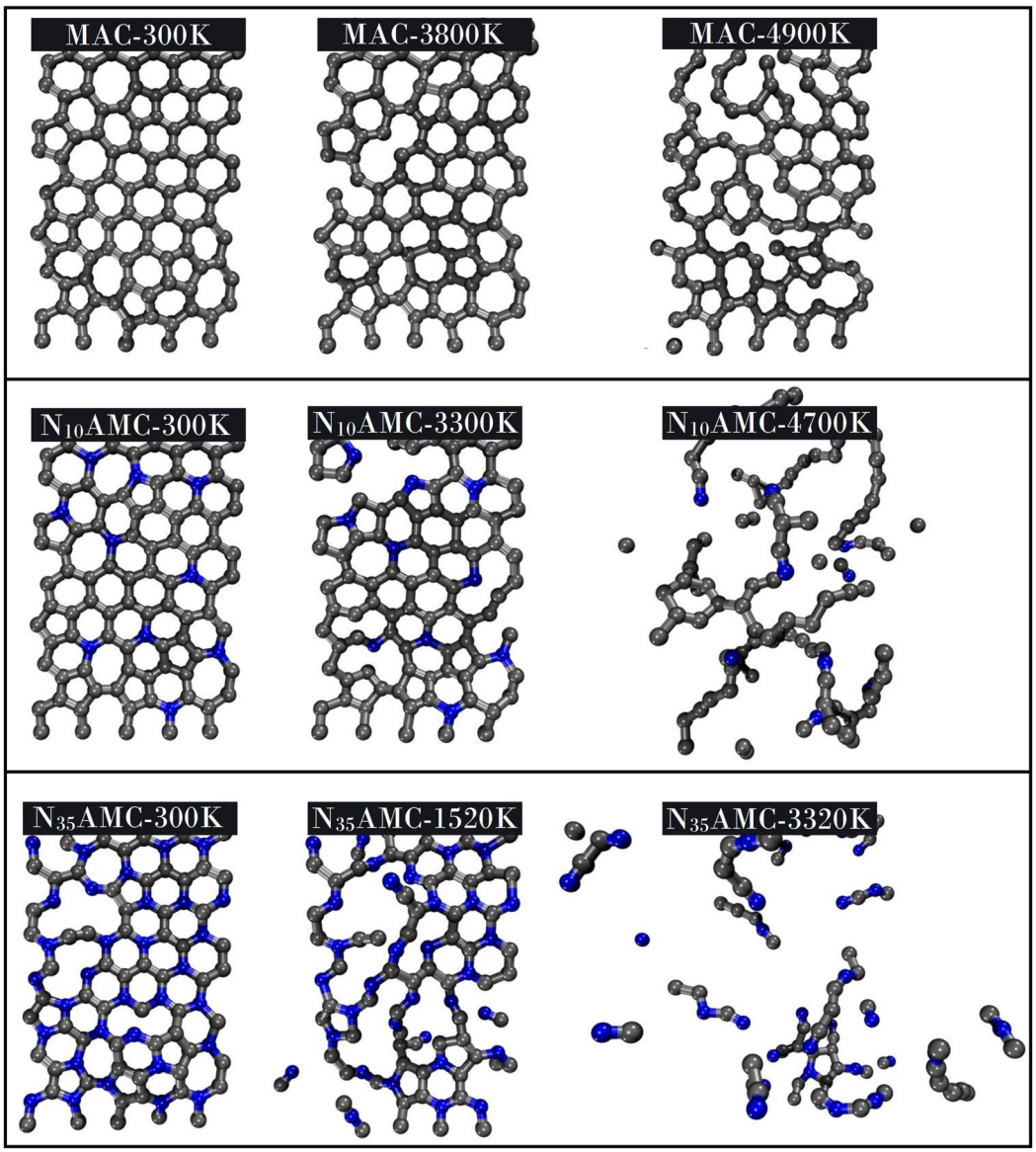

Fig. 7 Representative snapshots from MD simulations illustrating the thermal stability of (top) MAC, (middle) N_{10}AMC, and (bottom) N_{35}AMC systems.

doped system and all distinct degrees of thermal fluctuations. Incorporating nitrogen into the amorphous carbon lattice introduces a different interplay between localized states and bonding interactions, requiring lower thermal energy to disrupt the network. As a result, the nitrogen-doped N_{10}AMC structure exhibits a slightly decreased resistance to thermal fluctuations, resulting in a lower temperature for loss of its stability. These critical temperatures for thermal stability are consistent with those reported for other MAC structures,[14,15] highlighting the inherent robustness of the amorphous carbon network.

At elevated temperatures, the N_{10}AMC system exhibits lattice atomization and the formation of linear atomic chains (LACs) around 4700 K, as seen in the sequence of snapshots illustrated in the middle row of Fig. 7. This phenomenon, characterized by the appearance of elongated chains of atoms, is not observed in the undoped MAC, even at a higher temperature of 4900 K. Nitrogen in the NAMC structure facilitates the LAC appearance by forming more flexible and less constrained bonding configurations when subjected to high thermal energy values. The nitrogen atoms can create localized regions of weaker bonds, allowing the carbon network to reconfigure into LACs as the structure destabilizes.

The N_{35}AMC case can be considered metastable at temperatures ranging from 100 K to 300 K. At these temperatures, some of the atomic bonds within the structure begin to reconfigure, which indicates that the lattice is under thermal strain. However, despite these reconfigurations, the atoms remain bonded, preventing the formation of LACs or atomization. This behavior suggests that while the system is not entirely stable, it maintains some structural integrity.

Additionally, within this temperature range, we can observe the presence of well-structured lattice domains where original MAC regions persist. However, the high nitrogen content introduces significant local strain and deformations, creating small holes or vacancies within the amorphous structure, as illustrated in the first snapshot of the bottom row of Fig. 7. These defects contribute to the system's metastability, creating points of localized instability without leading to a complete breakdown/fracture of the overall structure. The combination of partial reconfiguration and the coexistence of stable domains with defects characterizes the metastable nature of the N_{35}AMC system.

The rapid destabilization of N_{35}AMC results from the high concentration of nitrogen atoms, which introduces considerable intrinsic strain and disorder into the MAC lattice, as discussed above. The increased number of nitrogen atoms disrupts the carbon–carbon bonds pattern, leading to a structure that cannot maintain its integrity even at relatively low thermal energies. As the temperature further increases, lattice atomization and the formation of LACs occur at around 1520 K, lower than the temperatures required for the undoped MAC and N_{10}AMC systems. The complete atomization of the N_{35}AMC system occurs at 3220 K.

Our study revealed some distinctive trends that set NAMC apart from MAC. One key observation is that NAMC exhibits a significant decrease in thermal stability as nitrogen doping increases, particularly at 35% doping, where the material becomes metastable at temperatures as low as 300 K. This behavior contrasts sharply with undoped MAC, which retains structural integrity up to approximately 3800 K, and nitrogen-doped graphene, which can sustain higher doping levels without such pronounced instability. The intrinsic disorder of the amorphous carbon network in MAC, combined with the localized electronic states introduced by nitrogen atoms, leads to increased strain and bond distortions at high doping levels, accelerating the onset of structural degradation. At moderate doping levels (*e.g.*, 10%), NAMC demonstrates a unique combination of structural flexibility and localized disruptions, which is not observed in undoped MAC or N-Gr. The nitrogen atoms alter the bonding environment, introducing perturbations that influence thermal response. These perturbations facilitate the formation of linear atomic chains at elevated temperatures, a phenomenon absent in undoped MAC and less pronounced in N-Gr. This behavior highlights the influence of nitrogen doping on the thermal dynamics of the amorphous structure. These trends suggest that NAMC offers tunable properties due to nitrogen incorporation, but its thermal stability is highly sensitive to doping concentration. This sensitivity differs from conventional amorphous carbon or graphene and underscores the importance of carefully optimizing doping levels for specific applications. We have added the sentence below to address this issue in the manuscript.

To summarize the discussion, the metastability of NAMC was determined through formation energy calculations and MD simulations conducted at 300 K, which revealed significant structural rearrangements and strain in the lattice, even at this relatively low temperature. While the system maintained some degree of structural coherence, localized bond breaking, and reconfigurations were observed, particularly around regions with higher nitrogen concentrations. These behaviors indicate that the material does not achieve an equilibrium state and instead exists in a metastable configuration prone to further structural changes under minor perturbations. The presence of local strain and defects, as evidenced by small vacancies and distortions in the lattice, further supports this conclusion.

This metastability implies potential limitations for practical applications of the 35% NAMC. For example, while the material may exhibit desirable electronic or optical properties at low temperatures, its structural integrity could degrade under operational conditions involving mechanical stress, thermal cycling, or prolonged exposure to environmental factors. Consequently, such high doping levels may restrict the material's suitability for applications requiring long-term stability, such as structural components in flexible electronics or optoelectronic devices. Instead, doping concentrations below 35%, where stability is preserved, are likely more practical for real-world applications. We have added the sentence below to address this issue in the manuscript.

4 Conclusions

In summary, we have investigated the recently synthesized nitrogen-doped monolayer amorphous carbon's structural, electronic, optical, and thermal properties using the DFTB+ approach. Our findings reveal that the maximum nitrogen concentration for achieving a stable NAMC structure is 35%, beyond which the lattice becomes structurally unstable. Nitrogen doping influences the formation energy values, which are consistently higher for NAMC than N-Gr for all concentration cases investigated here. This trend is attributed to the disordered nature of the amorphous carbon network in NAMC, which experiences more significant strain and bond rearrangement upon nitrogen incorporation than the graphene case.

Undoped MAC retains a metallic character with a Dirac-like cone. Upon nitrogen doping, it disappears. The doping also creates a significant number of localized states. Optical absorption spectra of MAC and NAMC systems show that nitrogen doping causes a redshift in the absorption spectra, broadening the range of optical activity. Undoped MAC displays strong absorption, mainly in the ultraviolet range. Undoped MAC and NAMC with 10% nitrogen doping exhibit considerably high thermal stability, with melting/vaporization temperatures of 3800 K and 3300 K, respectively. At 35% nitrogen doping, NAMC shows a significant decrease in structural stability, being metastable for temperatures ranging from 100 K up to 300 K, caused by increased structural disorder. The estimated Young's modulus values for the undoped MAC and N_{10}AMC are about 409.4 GPa and 416.4 GPa, respectively.

Author contributions

E. J. A. S: data curation, software, formal analysis, visualization. M. L. P. J.: formal analysis, investigation, validation, visualization, writing – review & editing, funding acquisition. R. M. T.: data curation, software, methodology, software, validation, investigation, data curation. D. S. G.: formal analysis, investigation, validation, writing – review & editing, funding acquisition. L. A. R. J.: conceptualization, methodology, formal analysis, investigation, resources, writing – review & editing, supervision, project administration, funding acquisition. All authors reviewed the manuscript.

Data availability

The data that support the findings of this study are available from the corresponding author, M. L. P. J., upon reasonable request.

Conflicts of interest

There are no conflicts to declare.

Acknowledgements

This work received partial support from the Brazilian agencies CAPES, CNPq, and FAPDF. M. L. P. J. acknowledges the financial support of the FAP-DF grant 00193-00001807/2023-16. The authors also acknowledge support from CENAPAD-SP (National High-Performance Center in São Paulo, State University of Campinas – UNICAMP, projects: proj950, proj634 and proj960) and NACAD (High-Performance Computing Center, Lobo Carneiro Supercomputer, Federal University of Rio de Janeiro – UFRJ, projects: a22002 and a23003) for the computational support provided. L. A. R. J. acknowledges the financial support from FAP-DF grants 00193.00001808/2022-71 and 00193-00001857/2023-95, FAPDF-PRONEM grant 00193.00001247/2021-20, and PDPG-FAPDF-CAPES Centro-Oeste grant 00193-00000867/2024-94. L. A. R. J. also acknowledges CNPq grants 350176/2022-1 and 167745/2023-9. D. S. G. acknowledges the Center for Computing in Engineering and Sciences at Unicamp for financial support through the FAPESP/CEPID grant #2013/08293-7.

References

1 A. Hirsch, *Nat. Mater.*, 2010, **9**, 868–871.
2 A. K. Geim, *Science*, 2009, **324**, 1530–1534.
3 S. Jana, A. Bandyopadhyay, S. Datta, D. Bhattacharya and D. Jana, *J. Phys.: Condens. Matter*, 2021, **34**, 053001.
4 R. Kumar, E. Joanni, R. K. Singh, D. P. Singh and S. A. Moshkalev, *Prog. Energy Combust. Sci.*, 2018, **67**, 115–157.
5 A. N. Enyashin and A. L. Ivanovskii, *Phys. Status Solidi B*, 2011, **248**, 1879–1883.
6 Q. Fan, L. Yan, M. W. Tripp, O. Krejčí, S. Dimosthenous, S. R. Kachel, M. Chen, A. S. Foster, U. Koert, P. Liljeroth, *et al.*, *Science*, 2021, **372**, 852–856.
7 L. Hou, X. Cui, B. Guan, S. Wang, R. Li, Y. Liu, D. Zhu and J. Zheng, *Nature*, 2022, **606**, 507–510.
8 E. Meirzadeh, A. M. Evans, M. Rezaee, M. Milich, C. J. Dionne, T. P. Darlington, S. T. Bao, A. K. Bartholomew, T. Handa, D. J. Rizzo, *et al.*, *Nature*, 2023, **613**, 71–76.
9 C.-T. Toh, H. Zhang, J. Lin, A. S. Mayorov, Y.-P. Wang, C. M. Orofeo, D. B. Ferry, H. Andersen, N. Kakenov, Z. Guo, *et al.*, *Nature*, 2020, **577**, 199–203.
10 H. Tian, Y. Ma, Z. Li, M. Cheng, S. Ning, E. Han, M. Xu, P.-F. Zhang, K. Zhao, R. Li, *et al.*, *Nature*, 2023, **615**, 56–61.
11 X. Bai, P. Hu, A. Li, Y. Zhang, A. Li, G. Zhang, Y. Xue, T. Jiang, Z. Wang, H. Cui, *et al.*, *Nature*, 2024, 1–5.
12 Y.-T. Zhang, Y.-P. Wang, X. Zhang, Y.-Y. Zhang, S. Du and S. T. Pantelides, *Nano Lett.*, 2022, **22**, 8018–8024.
13 W.-J. Joo, J.-H. Lee, Y. Jang, S.-G. Kang, Y.-N. Kwon, J. Chung, S. Lee, C. Kim, T.-H. Kim, C.-W. Yang, *et al.*, *Sci. Adv.*, 2017, **3**, e1601821.
14 L. C. Felix, R. M. Tromer, P. A. Autreto, L. A. Ribeiro Junior and D. S. Galvao, *J. Phys. Chem. C*, 2020, **124**, 14855–14860.

15 M. L. P. Junior, W. F. da Cunha, D. S. Galvão and L. A. Ribeiro Jr, *Phys. Chem. Chem. Phys.*, 2021, **23**, 9089–9095.
16 N. Gastellu, M. Kilgour and L. Simine, *J. Phys. Chem. Lett.*, 2022, **13**, 339–344.
17 R. Xia, S. Chen, S. Jiang, J. Zhang, X. Wang, C. Sun, Y. Xiao, Y. Liu and M. Gao, *ACS Appl. Mater. Interfaces*, 2020, **13**, 1114–1126.
18 A. J. Garzón-Ramírez, N. Gastellu and L. Simine, *J. Phys. Chem. Lett.*, 2022, **13**, 1057–1062.
19 P. Avouris and C. Dimitrakopoulos, *Mater. Today*, 2012, **15**, 86–97.
20 B. Mortazavi, M. Shahrokhi, A. V. Shapeev, T. Rabczuk and X. Zhuang, *J. Mater. Chem. C*, 2019, **7**, 10908–10917.
21 B. Mortazavi, M. Shahrokhi, M. Raeisi, X. Zhuang, L. F. C. Pereira and T. Rabczuk, *Carbon*, 2019, **149**, 733–742.
22 B. Mortazavi, M. Makaremi, M. Shahrokhi, Z. Fan and T. Rabczuk, *Carbon*, 2018, **137**, 57–67.
23 B. Mortazavi, *Materials*, 2023, **16**, 6642.
24 B. Mortazavi, F. Shojaei, M. Shahrokhi, M. Azizi, T. Rabczuk, A. V. Shapeev and X. Zhuang, *Carbon*, 2020, **167**, 40–50.
25 B. Mortazavi, *Carbon*, 2021, **182**, 373–383.
26 B. Mortazavi, F. Shojaei, M. Yagmurcukardes, A. V. Shapeev and X. Zhuang, *Carbon*, 2022, **200**, 500–509.
27 J. Wu, M.-T. F. Rodrigues, R. Vajtai and P. M. Ajayan, *Adv. Mater.*, 2016, **28**, 6239–6246.
28 N. Talukder, Y. Wang, B. B. Nunna and E. S. Lee, *Carbon*, 2021, **185**, 198–214.
29 B. Hourahine, B. Aradi, V. Blum, F. Bonafe, A. Buccheri, C. Camacho, C. Cevallos, M. Deshaye, T. Dumitrică, A. Dominguez, *et al.*, *J. Chem. Phys.*, 2020, **152**, 124101–124120.
30 B. Aradi, B. Hourahine and T. Frauenheim, *J. Phys. Chem. A*, 2007, **111**, 5678–5684.
31 M. Gaus, A. Goez and M. Elstner, *J. Chem. Theory Comput.*, 2013, **9**, 338–354.
32 M. Gaus, X. Lu, M. Elstner and Q. Cui, *J. Chem. Theory Comput.*, 2014, **10**, 1518–1537.
33 G. Seifert, *J. Phys. Chem. A*, 2007, **111**(26), 5609–5613.
34 I. Mitchell, B. Aradi and A. J. Page, *J. Comput. Chem.*, 2018, **39**, 2452–2458.
35 Y. Chen, M. Liu, J. Chen, Y. Li, C. Zhao and X. Mu, *Appl. Surf. Sci.*, 2018, **458**, 454–463.
36 B. Hourahine, B. Aradi and T. Frauenheim, *J. Phys.:Conf. Ser.*, 2010, 012005.
37 Z. Shen, R. I. Sosa, S. P. Bordas, A. Tkatchenko and J. Lengiewicz, *Int. J. Eng. Sci.*, 2024, **204**, 104126.
38 A. Luo and J. Chen, *Colloids Surf., A*, 2024, **688**, 133651.
39 G. S. Fabris, D. S. Galvão and R. Paupitz, *Phys. Chem. Chem. Phys.*, 2024, **26**, 11589–11596.
40 R. Podeszwa, W. Jankiewicz, M. Krzuś and H. A. Witek, *J. Chem. Phys.*, 2019, **150**, 234110.
41 A. Khemissi and H. Khalfoun, *Diamond Relat. Mater.*, 2023, **140**, 110436.
42 S. Panahi, M. Jamaati and A. Namiranian, *Mater. Sci. Eng., B*, 2021, **268**, 115118.
43 A. Zobelli, V. Ivanovskaya, P. Wagner, I. Suarez-Martinez, A. Yaya and C. P. Ewels, *Phys. Status Solidi B*, 2012, **249**, 276–282.
44 X. Wang and L. Zhang, *Mater. Today Commun.*, 2024, 110382.
45 C. E. Junkermeier and R. Paupitz, *Comput. Mater. Sci.*, 2019, **164**, 31–38.
46 S. K. Kim, W. Chen, S. Pourasad and K. S. Kim, *J. Phys. Chem. C*, 2016, **120**, 19212–19224.
47 N. Shuichi, *Prog. Theor. Phys. Suppl.*, 1991, **103**, 1–46.
48 A. Krishnapriyan, P. Yang, A. M. N. Niklasson and M. J. Cawkwell, *J. Chem. Theory Comput.*, 2017, **13**, 6191–6200.
49 N. Goldman, S. Goverapet Srinivasan, S. Hamel, L. E. Fried, M. Gaus and M. Elstner, *J. Phys. Chem. C*, 2013, **117**, 7885–7894.
50 W. Sun, G. Fan, T. van der Heide, A. McSloy, T. Frauenheim and B. Aradi, *J. Chem. Theory Comput.*, 2023, **19**, 3877–3888.
51 L. Wei, D. Zhao, J. Li, J. Liu and L. Zhang, *Diamond Relat. Mater.*, 2021, **116**, 108383.
52 Y. Pang and M. Springborg, *Comput. Mater. Sci.*, 2016, **118**, 203–213.
53 V. T. Barone and B. R. Tuttle, *AIP Adv.*, 2020, **10**, 105115.
54 R. M. Tromer, L. C. Felix, L. A. Ribeiro and D. S. Galvao, *Phys. E*, 2021, **130**, 114683.
55 Z. Shi, A. Kutana and B. I. Yakobson, *J. Phys. Chem. Lett.*, 2015, **6**, 106–112.
56 M. Kaukonen, R. M. Nieminen, S. Pöykkö and A. P. Seitsonen, *Phys. Rev. Lett.*, 1999, **83**, 5346–5349.
57 X. Li, K. Hou, D. Qiu, P. Yi and X. Lai, *Carbon*, 2020, **167**, 219–229.
58 B. Zheng, W. Zheng, K. Zhang, Q. Wen, J. Zhu, S. Meng, X. He and J. Han, *Carbon*, 2006, **44**, 962–968.
59 J. Schwan, V. Batori, S. Ulrich, H. Ehrhardt and S. R. P. Silva, *J. Appl. Phys.*, 1998, **84**, 2071–2081.
60 V. S. Veerasamy, J. Yuan, G. A. J. Amaratunga, W. I. Milne, K. W. R. Gilkes, M. Weiler and L. M. Brown, *Phys. Rev. B: Condens. Matter Mater. Phys.*, 1993, **48**, 17954–17959.
61 R. M. Tromer, M. L. P. Júnior, L. A. Ribeiro Jr and D. S. Galvão, *Chem. Phys. Lett.*, 2024, 141647.
62 B. Wang, Q. Wu, Y. Zhang, L. Ma and J. Wang, *ACS Appl. Mater. Interfaces*, 2019, **11**, 33231–33237.
63 Y. Zhao, X. Li, J. Liu, C. Zhang and Q. Wang, *J. Phys. Chem. Lett.*, 2018, **9**, 1815–1820.
64 F. Mouhat and F.-X. Coudert, *Phys. Rev. B:Condens. Matter Mater. Phys.*, 2014, **90**, 224104.
65 Y. Ying, K. Fan, S. Zhu, X. Luo and H. Huang, *J. Phys. Chem. C*, 2020, **124**, 639–646.
66 J. Hu, H. Zeng, C. Wang, Z. Li, C. Kan and Y. Liu, *Phys. Chem. Chem. Phys.*, 2014, **16**, 23483–23491.
67 B. Mortazavi, S. Ahzi, V. Toniazzo and Y. Rémond, *Phys. Lett. A*, 2012, **376**, 1146–1153.
68 X. Wang, L. Chen, Z. Yuan, J. Rong, J. Feng, I. Muzammil, X. Yu, Y. Zhang and Z. Zhan, *J. Mater. Chem. A*, 2019, **7**, 8967–8974.